Modeling of Wave Propagation through Soft Electrically Tunable Metamaterials

Michael A. Jandron[1,2] and David Henann[2]

[1]Naval Undersea Warfare Center Division Newport, Newport, RI
[2]School of Engineering, Brown University, Providence, RI

***Abstract**: In this paper, we present our numerical simulation capability, developed within the Abaqus/Standard environment, for modeling steady-state wave propagation through soft dielectric elastomer composites. Specifically, we will discuss (a) a nonlinear user-element subroutine (UEL) to simulate the coupled electric-displacement response of these soft materials, (b) a user MPC subroutine to enforce complex-valued Bloch-Floquet constraints, as well as to impose appropriate updated Lagrangian boundary conditions on the representative volume element (RVE), and (c) a method within the UEL to lower the dispersion error in the solution by modifying the mass matrix. Through the combination of these methods, we can study how the application of an electric field to these materials results in opening and closing of phononic band-gaps, that is, frequency ranges in which propagating waves through the dielectric elastomer composite are not permitted. This modeling framework is useful to guide the development of phononic metamaterials that cannot be studied analytically and leverages the computational backbone of Abaqus/Standard, which enhances portability and maintainability of our modeling approach. We envision using these electrically-tunable phononic metamaterials to provide vibration isolation for undersea structures. This work is supported through the Naval Undersea Warfare Center In-house Laboratory Independent Research (ILIR) program.*

***Keywords**: Wave Propagation, Dielectric Elastomers, Gent, Hyperelasticity, Phononic Crystals, Dispersion, Band Gaps, Bloch-Floquet, Representative Volume Element.*

1. Introduction

A solid phononic crystal exhibits shear and longitudinal propagating waves which can harness constructive interference through Bragg scattering (see e.g., Lai, 2001). Interest in these materials has grown in recent years, and small-strain (e.g. metallic or ceramic) phononic crystals have been extensively researched. Tunability of small-strain phononic crystals has been explored using piezoelectrics (Oh, 2011) and magneto-elastics (Vasseur, 2011, Matar, 2012), but because of the high wave speeds, the physical dimensions of the resulting phononic crystals tend to be large. Soft materials offer the advantage of lower shear wave speeds which do not require very large unit cell dimensions. Since elastomers exhibit non-linear elastic material behavior, it is straightforward to change stiffness properties of the unit cell through large deformation, thereby changing the speed of wave propagation. This route to achieving tunability is just beginning to be explored. For instance, Bertoldi and Boyce (2008) demonstrated significant band gap dependence on finite pre-deformations in very soft elastomeric phononic crystals containing voids. They noted that by using an externally applied force to deform the unit cell, opening and closing of band gaps was observed. In some cases, they opened total band gaps, which block all shear wave polarizations.

Dielectric elastomers (DEs) offer a unique way to couple the large reversible deformations required for tunability with an externally applied electric field. DEs began appearing in the literature in the late 1990s (Pelrine, 1998, 2000). They deform significantly when a voltage is applied through a set of complaint surface-mounted electrodes. DEs are different from piezoelectric materials in that piezoelectrics typically only undergo small deformations, possess a linear relation of electric field to stress, and are polar crystalline solids. DEs, on the other hand, undergo large deformations, possess a quadratic relation between electric field and stress, and are non-polar amorphous materials. Research in using DEs for phononic crystals was discussed by Shmuel (2012) who developed analytical solutions for elastic wave propagation in a one dimensional periodic laminate undergoing large homogeneous deformations in response to an electric field. Shmuel (2013) expanded on this work by deriving analytical solutions for a DE composite made up of an array of cylindrical fibers in a matrix, but this was again limited to homogeneous pre-deformations.

Numerical prediction methods are required for applications involving inhomogeneous deformations, but these approaches are largely new to DEs (Vu, 2007, Henann, 2013). We are currently using a User Element (UEL) subroutine within the Abaqus/Standard environment, developed by Henann (2013), to solve for the coupled electro-mechanical response of the composite solid. In the present work, we have extended this code to be compatible with an Abaqus natural frequency extraction analysis step. In addition, we have included complex-valued Bloch-Floquet boundary conditions on the periodic solid using a user defined MPC subroutine. Finally, to obtain higher order accuracy for a given finite element mesh, we have implemented a modification to the calculation of the mass matrix (also through the UEL subroutine) to reduce wavenumber dispersion (Jandron, 2015).

The outline of this paper is as follows. Section 2 summarizes the coupled electro-mechanical constitutive model that is implemented in the UEL. Section 3 discusses the RVE-based modeling approach and associated MPC constraints. Section 4 summarizes the modifications made to the mass matrix in order to lower dispersion. Section 5 shows some representative results utilizing this approach including a verification of the new mass integration scheme. And finally, Section 6 summarizes the main points of this work and gives an outlook into future efforts.

2. Coupled Electric-Displacement Theory

A very brief summary of the theory involved in the solution of the coupled electro-mechanical response for the dielectric elastomers is presented. Further descriptions are contained in McMeeking and Landis (2005, 2007), Dorfmann, Ogden, and Bustamante (2005, 2009, 2010, 2014) Suo, Zhao, and Greene (2008), Henann et al. (2013), and references contained therein.

Consider the mapping shown in Fig. 1, $\boldsymbol{x} = \mathcal{X}(\mathbf{X}, t)$ which maps a reference material particle $\mathbf{X}$ to a current position $\boldsymbol{x}$. The deformation gradient is $\boldsymbol{F} = \boldsymbol{\nabla X}$, which can be decomposed through the polar decomposition theorem as a stretch followed by a rotation, $\boldsymbol{F} = \boldsymbol{RU}$. The volume change is defined by the Jacobian, $J = \det \boldsymbol{F}$ and left/right Cauchy-Green stress tensors are $\boldsymbol{B} = \boldsymbol{F}\boldsymbol{F}^T$ and $\boldsymbol{C} = \boldsymbol{F}^T\boldsymbol{F}$, respectively.

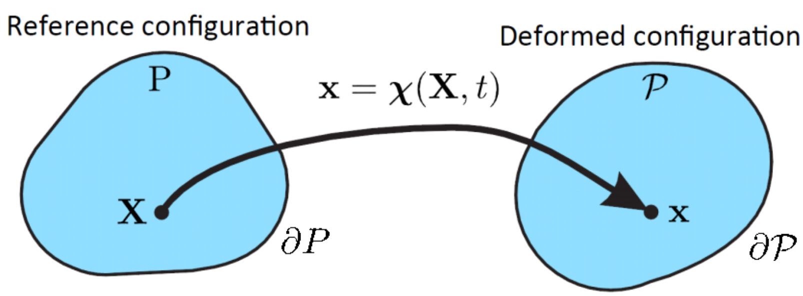

Figure 1. Mapping of a material part from the reference to the current configuration.

In the current configuration, the mechanical response is governed by the conservation of momentum,

$$\nabla \cdot \boldsymbol{\sigma} + \boldsymbol{b} = \mathbf{0} \qquad \text{(in } P\text{)}$$
$$\boldsymbol{\sigma} \cdot \boldsymbol{n} = \boldsymbol{t} \qquad \text{(on } \partial P\text{)}$$

where $\boldsymbol{\sigma}$ is the Cauchy stress, **b** is the body force, $\boldsymbol{n}$ is outward unit vector normal to the surface boundary, and $\boldsymbol{t}$ is the applied traction vector on the surface boundary.

The electrical response is assumed electrostatic and is governed by two of Maxwell's equations: Gauss's law and Faraday's law. Faraday's law is satisfied if the electric field in the material is given through the gradient of the voltage field, φ as,

$$\boldsymbol{E} = -\nabla\varphi \qquad \text{(in } P\text{)}$$

Gauss's law relates the electric displacement vector, $\boldsymbol{D}$, to the volumetric free charge density, q, in the dielectric and to the surface free change density, ω, on the boundary surface as,

$$\nabla \cdot \mathbf{D} = q \qquad \text{(in P)}$$
$$\mathbf{D} \cdot \boldsymbol{n} = -\omega \qquad \text{(on } \partial\text{P)}$$

The constitutive response for a time-independent dielectric elastomer is entirely given through a free energy function. (For a complete discussion of the thermodynamics of DEs, see Henann et al. (2013).) The free energy can be expressed through a hyperelastic constitutive law, e.g., a Neo-Hookean, Gent, or Arruda-Boyce model, for the mechanical response and an equation of state for the dielectric material (typically taken to be an ideal dielectric). This yields a set of constitutive equations relating the electrical and mechanical behavior of the material.

For example, for the case of a free energy function consisting of a Gent rubber hyperelasticity model and the ideal dielectric, the *Cauchy stress* in the material is given by,

$$\boldsymbol{\sigma} = \mu\left(\mathbf{1} - \frac{I_1 - 3}{I_m}\right)^{-1} \boldsymbol{B} + \epsilon \boldsymbol{E} \otimes \boldsymbol{E} - P\mathbf{1}$$

where μ is the initial shear modulus, $I_1 = trace(\boldsymbol{B})$, I_m is a Gent material parameter (henceforth just I will be used since the subscript notation will be reserved for the material in the unit cell) denoting the stiffening effect of polymer chains in the elastomer, ϵ is the electric permittivity of the dielectric elastomer, P is the pressure, and $\boldsymbol{1}$ is the identity tensor. Similarly, the electric displacement in the material is related to the electric field by,

$$\mathbf{D} = \epsilon \boldsymbol{E}.$$

A finite element implementation can be developed utilizing nodal displacement degrees of freedom for the mechanical response and an electric potential degree of freedom for the electric behavior. Because the problem is non-linear due to finite deformations and non-linear material behavior, a Newton-Raphson iterative scheme can be employed. Element-level residuals and tangents can be coded into a user defined element (UEL) subroutine and solved with Abaqus (c.f., Henann, 2013).

3. Periodic Constraints

In the cases of periodic structures (or even statistically periodic) it is convenient to define a single unit cell with appropriate boundary conditions to represent the macroscopic behavior of the overall structure. This approach is commonly referred to as the Representative Volume Element (RVE) approach. It was originally developed for micromechanical plasticity models (Tvergard, 1982, Socrate, 1995) then polymeric composites (Danielsson, 2002, Parsons, 2006) but can also be applied to phononic crystal research (Bertoldi, 2008).

A key concept in the RVE approach is the addition of three virtual nodes which can be used to prescribe a macroscopic deformation gradient,

$$\begin{bmatrix} F_{11}-1 & F_{12} & F_{13} \\ F_{21} & F_{22}-1 & F_{23} \\ F_{31} & F_{32} & F_{33}-1 \end{bmatrix} = \begin{bmatrix} u_1|_{node1} & u_2|_{node1} & u_3|_{node1} \\ u_1|_{node2} & u_2|_{node2} & u_3|_{node2} \\ u_1|_{node3} & u_2|_{node3} & u_3|_{node3} \end{bmatrix}.$$

This means, if nodes A and B are a periodic pair, their displacements, $\boldsymbol{u}|_A, \boldsymbol{u}|_B$, are related through

$$\boldsymbol{u}|_B - \boldsymbol{u}|_A = (\boldsymbol{F} - \mathbf{1})\{\boldsymbol{X}|_B - \boldsymbol{X}|_A\}$$

where $\boldsymbol{F}$ is the macroscopic deformation gradient and $\boldsymbol{X}$ is the position in the reference configuration. The more challenging aspect, however, is enforcing the complex-valued Bloch-Floquet constraints which are required to model wave propagation in the solid. For a 1D solid, this constraint is simply

$$u(A) = u(B)e^{-ik_x L}$$

where A is the left most side, B is the right most side, k_x is the wavenumber in the x-direction, L is the length of the solid, and $i = \sqrt{-1}$. Then, by imposing k_x a complex valued relation between $u(A)$ and $u(B)$ is known. Applying this type of constraint requires that the finite element mesh be duplicated into a real and an imaginary mesh. Then, the MPC user subroutine is used to relate these otherwise disconnected meshes and enforce this constraint. This approach extends to the 3D cases considered in the present work.

4. Scheme for Reduced Dispersion

Since our interest is in extracting natural frequencies, we are concerned with the error of the resolved wavelength compared to the exact solution which is known to become worse as wavelength decreases since there will be less nodal degrees of freedom per wavelength. This is commonly referred to as dispersion error. Hughes (2000) was one of the earliest to realize that the choice in how the mass matrix is computed can reduce dispersion. He noted that by using a lumped mass scheme the finite element solution exhibits a phase *lag* compared to the exact solution, and conversely by using a consistent mass scheme the finite element solution exhibits a phase *lead* compared to the exact solution. He also noted that by using a simple average of both schemes gives two orders more accuracy. However, in most finite element implementations, the computational cost associated with assembling both of these schemes becomes excessive. By default Abaqus/Standard uses a lumped mass formulation for lower-order elements, but not for higher-order elements, and in Abaqus/Explicit lumped masses are always used. There are advantages to lumped or diagonal mass matrices for explicit dynamics where the mass matrix changes and needs to be inverted at every time step, but there is minimal advantage in an implicit scheme. Recently the work of Challa (1998), Guddati (2004), and Ainsworth (2010) showed that it was possible to modify the integration quadrature scheme and obtain one full order of accuracy boost without any increased computational cost. An explicit construction of the integration points and weights is described in Ainsworth (2010) and the final result is described here for completeness. First, the roots of the Legendre Polynomial are used to give the integration points $\{\xi_i\}_{i=0}^{p}$,

$$L'_{p+1}(\xi_i) - \tau L'_{p-1}(\xi_i) = 0$$

where $L'_p(\xi_i)$ denotes the first derivative of the Legendre polynomial of order p and τ is the optimal blending parameter, $\tau = p/(p+1)$. Once these points are known, we compute the associated weights using,

$$w_i = \frac{2[p(1+\tau)+\tau]}{p(p+1)L_p(\xi_i)\left[L'_{p+1}(\xi_i) - \tau L'_{p-1}(\xi_i)\right]}$$

Then these points and weights are used to numerically approximate the following integral,

$$\int_{-1}^{1} f(x)dx = \sum_{i=1}^{n} w_i f(x_i)$$

This result easily extends to higher dimensions by using a tensor product of these points and weights. These are computed and tabulated in Ainsworth (2010) and again in Jandron (2015) but a summary of these are presented in Table 1 below. It is termed the optimally blended integration scheme by Ainsworth.

Table 1. Optimally Blended Integration Points and Weights

Order, p	Abscissas, ξ_i	Weights, w_i
1	± 0.8164965809277260	1
2	0	1.2307692307692306
	± 0.9309493362512628	0.3846153846153845
3	± 0.4293520583157873	0.8001739855520776
	± 0.9643352758795620	0.1998260144479225

Jandron (2015) implemented this new quadrature scheme into an Abaqus UEL suitable for 1D, 2D, and 3D continuum elements of various order. Using this UEL with Abaqus, we were able to improve accuracy with no additional computational cost. The error originally present at ten nodes per wavelength was now present at four nodes per wavelength. As a result, this UEL has been incorporated into the present work so that a coarser mesh can be used to obtain similar orders of accuracy at a smaller computational cost.

5. Results

In order to demonstrate all aspects of our numerical simulation capability, we consider a representative composite material made up of cylindrical inclusions (*i*) arranged on a square lattice in the matrix (*m*), so that the periodic unit cell of the composite takes the form shown in Fig. 2, right. The periodic unit cell is modeled in Abaqus using a generalized plane strain setting to allow for out-of-plane shear wave polarizations. This is achieved by utilizing one continuum element in the out-of-plane direction. The RVE may first be subjected to large pre-deformations, utilizing the virtual nodes, followed natural frequency extraction analyses. For the natural frequency steps, the complex-valued Bloch-Floquet boundary conditions are prescribed through the MPC user subroutine, using an approach that splits the real and imaginary variables. Since the Bloch-Floquet constraint is dependent on wavenumber, we perform multiple Abaqus/Standard natural frequency extraction steps where a different wavenumber is applied in each step, which corresponds to tracing the boundary of the irreducible Brillouin zone (Srivastava, 1990) as shown in Fig. 2, left. The wavevector is varied through the MPC subroutine and natural frequencies are extracted which are later used to construct the phononic band structure. This approach is also described in more detail in Bertoldi (2008).

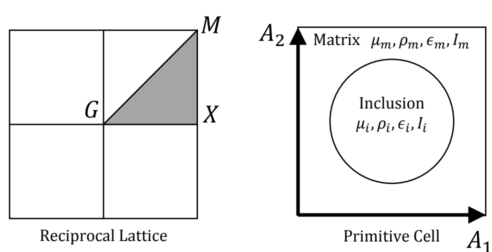

Figure 2. Reciprocal lattice and primitive cell used in RVE and Bloch-Floquet constraints. We take $A_1 = A_2 = A = 1$ for all work in this paper.

For material properties: ρ is the mass density, ϵ is the dielectric permittivity, I is a material parameter for the Gent hyperelasticity model, μ is the elastic shear modulus, and K is the elastic bulk modulus. It is assumed that $K/\mu = 1000$ for the analysis to represent approximate incompressibility.

Our first task is to illustrate the increased accuracy obtained by utilizing the blended mass scheme with reduced dispersion error. We compare results obtained using the default Abaqus mass integration scheme with those obtained using the blended integration scheme for a case in which the exact solution of the phononic band structure is known. The exact solution follows from Shmuel (2013) where he computed the band structure for shear waves with out-of-plane polarization for dielectric elastomers subjected to static, large, homogeneous out-of-plane pre-deformations (i.e., parallel to the cylinder axis). Shmuel's approach was to modify the result of Kushwaha (1993) and Kushwaha (1994), who developed the solution for infinitesimal deformations, by accounting for the increase in μ caused by electrically induced deformation.

Fig. 3 left shows results obtained using the default Abaqus/Standard C3D8-element mass-matrix integration scheme compared to the exact out-of-plane solution while Fig. 3 right shows results obtained using the blended mass integration scheme compared to the exact out-of-plane solution. The in-plane wave polarizations are shown on the left of each band diagram for reference but an exact solution cannot be derived for this case. The properties are defined by $\frac{\epsilon_i}{\epsilon_m} = 10$, $\frac{\mu_i}{\mu_m} = 10$, $\frac{\rho_i}{\rho_m} = 1$, $I_i = I_m = 10$, and an in-plane equibiaxial pre-stretch of $\lambda = 1.2$ is applied. These figures are directly compariable to Shmuel (2013) Figure 2b except a higher number of plane waves $(-50 \leq n_1, n_2 \leq 50)$ is used in the wavenumber expansion (see e.g., Kushwaha 1993) which generates a more converged analytical solution. The difference between the default integration scheme vs. the blended scheme become noticeable as wavenumbers increase (increasing along y-axis), and since there is no additional computational cost – the method is attractive.

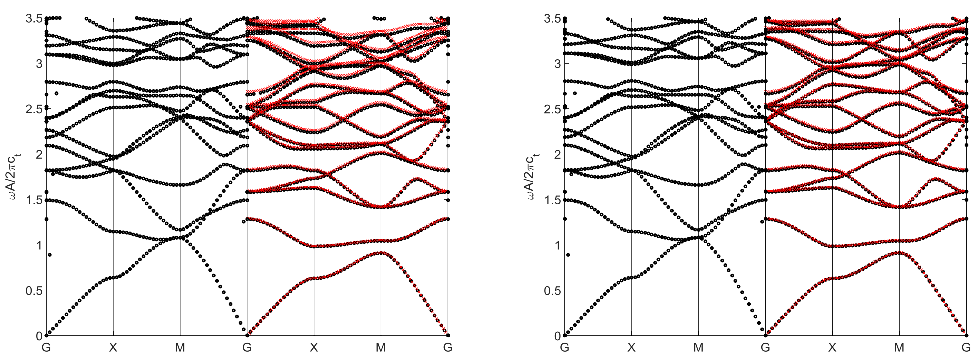

Figure 3. Effect of higher order blended integration mass matrix. Left refers to mass matrix using the default lower-order element in Abaqus/Standard (C3D8) and right refers to the mass matrix using the blended integration scheme. Finite element results are shown as black circles and red x's refer to exact solutions. Left and right sections of each plot refer to in-plane and out-of-

plane wave polarizations, respectively. Stray circles represent bulk waves which are still present in the solid because $K/\mu = 1000$. Solution parameters $\frac{\epsilon_i}{\epsilon_m} = 10, \frac{\mu_i}{\mu_m} = 10, \frac{\rho_i}{\rho_m} = 1, I_i = I_m = 10$, and an in-plane equibiaxial prestretch of $\lambda = 1.2$. Also ω denotes circular frequency, A denotes the unit cell dimension, and c_t denotes the shear wave speed in the matrix material $c_t = \sqrt{\mu_m/\rho_m}$ (computed using $\mu_m = 2e6, \rho_m = 1000$).

Next, we study the effect of material properties on the response of the representative phononic crystal composite. Our analysis proceeds in two steps: (1) a quasi-static analysis, in which large pre-deformation is attained through the application of a far-field electric field and (2) a set of natural frequency extraction steps for different wavenumbers in order to construct the dispersion diagram. Focusing on the first step, consider the case with a shear modulus mismatch of $\frac{\mu_i}{\mu_m} = 10$. Fig. 4 left shows how an applied normalized electric field, $\frac{\phi}{A}\sqrt{\frac{\bar{\epsilon}}{\bar{\mu}}}$ (e.g., see Henann, 2013), in the horizontal direction affects the macroscopic stretch λ in the unit cell for different values of $\frac{\epsilon_i}{\epsilon_m}$. Here, $\bar{\epsilon}$ is the volume averaged electric permittivity, $\bar{\epsilon} = v_f \epsilon_i + (1 - v_f)\epsilon_m$, $\bar{\mu}$ is the volume averaged shear modulus, ϕ is the voltage difference applied to the unit cell, and A is again the undeformed unit cell length. From Fig. 4 left we see that $\frac{\epsilon_i}{\epsilon_m} = 1$ requires the least amount of electric potential to reach $\lambda = 1.125 \pm 0.0001$ (this was achieved through a UAMP subroutine), and increasing electric potential is required to reach a given stretch as $\max\left(\frac{\epsilon_i}{\epsilon_m}, \frac{\epsilon_m}{\epsilon_i}\right)$ increases.

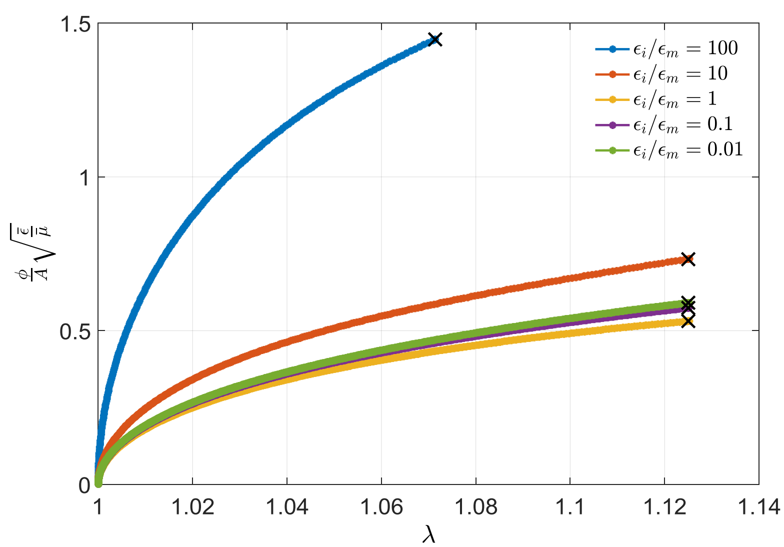

Figure 4. Normalized electric potential versus vertical stretch. Black x's denote final solution. All cases reach the goal of $\lambda = 1.125 \pm 0.0001$ except $\frac{\epsilon_i}{\epsilon_m} = 100$ because of mesh distortion.

Fig. 5 shows field results of electric potential ϕ and maximum principle logarithmic strain ε after the electric field has been applied which results in a vertical stretch of $\lambda = 1.125 \pm 0.0001$. The $\frac{\epsilon_i}{\epsilon_m} = 1$ case shows the most elliptical inclusion shape, the minimum amount of strain overall, as well as minimum strain on the left and right sides of the inclusion. For $\frac{\epsilon_i}{\epsilon_m} = 10$ substantial strain in the matrix material on the sides of the inclusion are evident. As a result of this, the inclusion shape is more circular. As $\frac{\epsilon_i}{\epsilon_m}$ further increases this effects continues and eventually mesh distortion causes the analysis to fail. For $\frac{\epsilon_i}{\epsilon_m} < 1$ we see similar effects. Hence, for the difference permittivity mismatches, different microscopic deformation is attained despite identical macroscopic deformation.

The effect of the microscopic differences in the deformation also affects the phononic band structure. Figs. 6 and 7 show the phononic band structure for $\frac{\mu_i}{\mu_m} = 10$ and $\frac{\mu_i}{\mu_m} = 100$, respectively. The blue regions represent frequency ranges in which out-of-plane shear waves do not propagate (i.e., band-gaps), yellow regions represent in-plane, and purple regions represent total band-gaps, that is, regions where both shear wave polarizations are prohibited. Each unactuated case is identical, as expected. However, differences emerge as ϕ increases for each $\frac{\epsilon_i}{\epsilon_m}$ case. Band-gaps appear to shift, open, and close. For comparison, we show band structures for the same macroscopic vertical stretch as the electric potential increases. Electric potential values are per unit cell.

Fig. 7 shows a situation in which the externally applied electric field causes a total band-gap to appear. Interestingly this total band-gap peaks around $\lambda = 1.075$ and vanishes in two of the three cases by $\lambda = 1.125$. We envision tunability through an externally applied electric field to obtain band-gaps in a frequency range of interest.

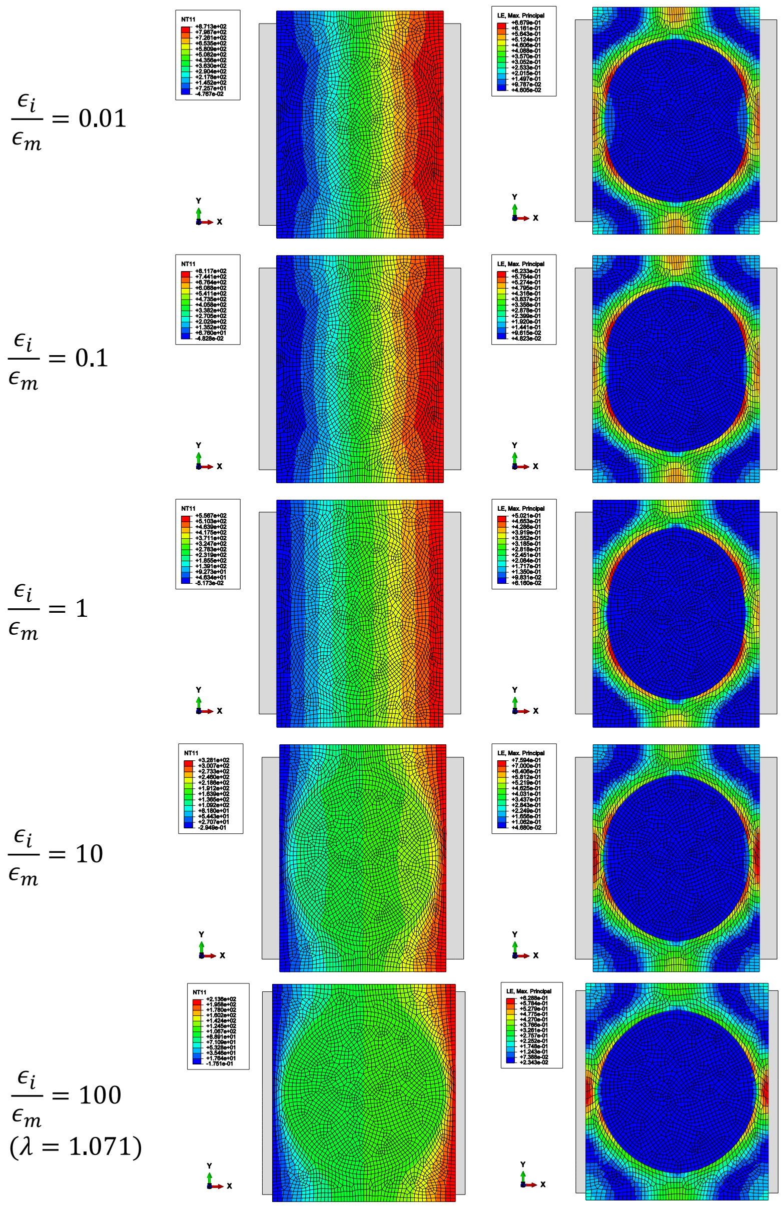

Figure 5. Effect of $\frac{\epsilon_i}{\epsilon_m}$ on microscopic deformations for $\frac{\mu_i}{\mu_m} = 10$ and an applied electric field that results in a vertical stretch of $\lambda = 1.125 \pm 0.0001$. $\frac{\epsilon_i}{\epsilon_m}$ increases from top to bottom. Left, electric potential ϕ solution, and right, maximum principle logarithmic strains ε in the unit cell.

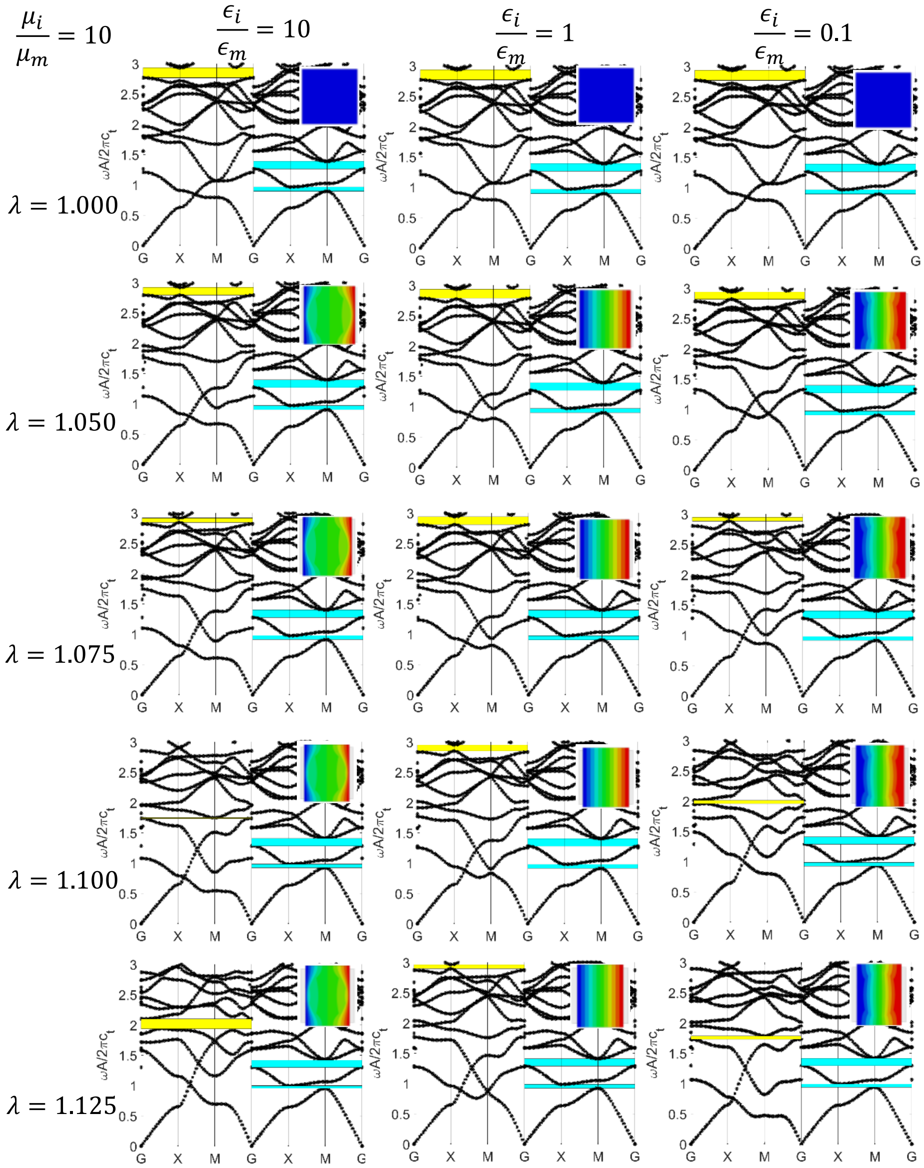

Figure 6. Dependence of the phononic band gap structure on $\frac{\epsilon_i}{\epsilon_m}$ and ϕ for $\frac{\mu_i}{\mu_m} = 10$. Note ϕ is applied until stated macroscopic λ is met. Left, in-plane; right, out-of-plane. Field results show contours of the electric potential in the unit cell.

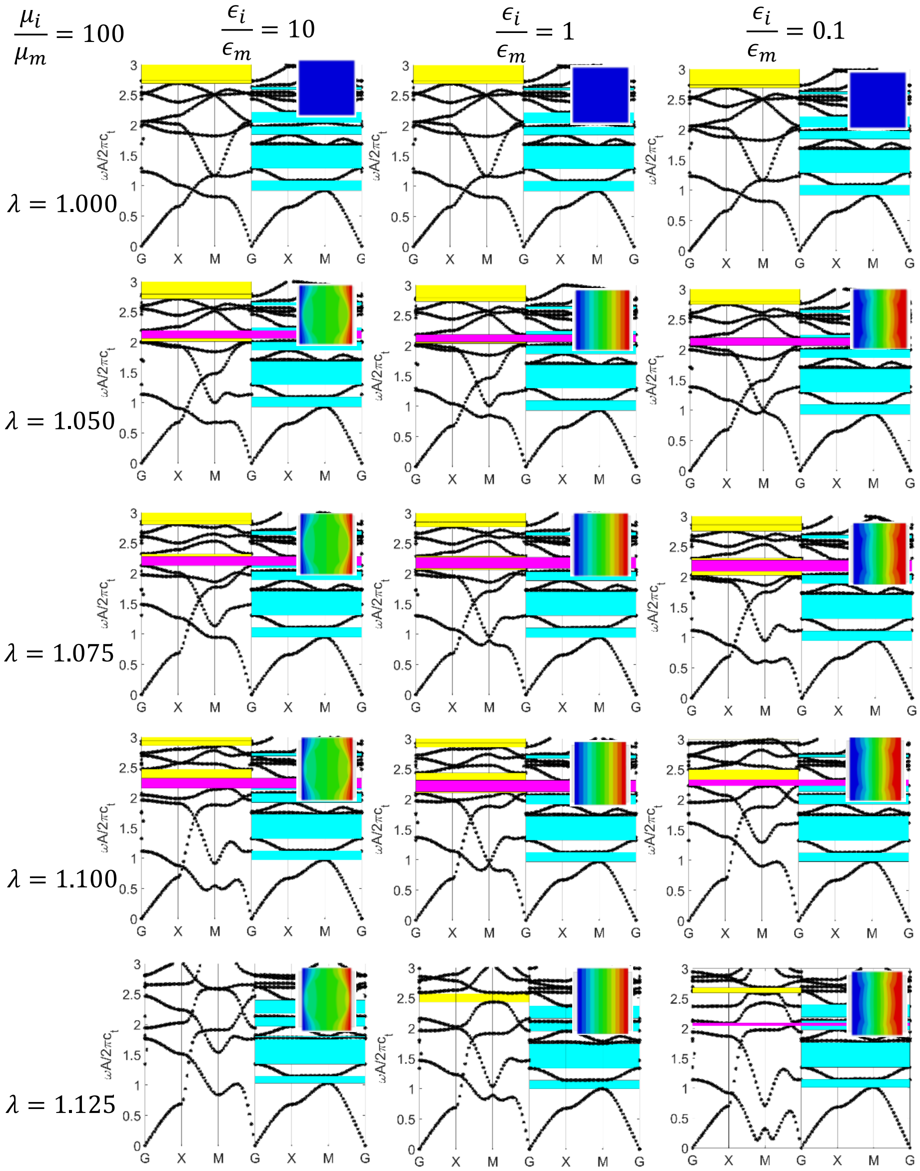

Figure 7. Dependence of the phononic band gap structure on $\frac{\epsilon_i}{\epsilon_m}$ and ϕ for $\frac{\mu_i}{\mu_m} = 100$. Note ϕ is applied until stated macroscopic λ is met. Left, in-plane; right, out-of-plane. Field results show contours of the electric potential in the unit cell.

Electric field direction (only a horizontally applied electric field was considered in the present work), volume fraction, inclusion shape and lattice arrangement will be considered in future work. Further study of the effect of electric permittivity mismatch on microscopic shape change is also warranted. We anticipate to leverage the work of Wang (2007) who showed that the largest complete band-gaps occur when the shape of the inclusion matches that of the lattice. Wang (2007) and Qian (2008) also show optimal volume fractions which give the largest first complete band-gap for various inclusion shapes and lattice arrangements. However, little is still known about how all of these studies extend into the finite deformation case. Much work is still to be done in this area, and especially what role these dielectric elastomers can have for tunability of phononic crystals.

6. Conclusions

In summary, we have made use of Abaqus/Standard to study wave propagation in electrically tunable soft phononic crystals. This was possible by extending the coupled electric-potential-displacement UEL subroutine developed by Henann (2013) to work with wave propagation problems. We have also developed an MPC subroutine to impose periodic boundary conditions on RVEs and to enforce complex-valued Block-Floquet conditions so that natural frequencies may be extracted for specified wavenumbers. Finally, we leveraged work from Jandron (2015) who developed an Abaqus/Standard UEL to achieve higher accuracy in resolving wavelength in wave propagation problems. All of these additions build up to a framework that we can use to explore the vast parameter space of phononic crystal tunability using dielectric elastomers.

In Section 5 we showed how an electric permittivity mismatch can be used to affect the deformation inside the unit cell under an applied electric field, and also how these results are heavily dependent on electric field strength. This was evident through the opening and closing of band-gaps even for the small amount of resulting vertical stretch $\lambda = 1.125$. The effect of shear modulus mismatch also strongly affects band-gaps, and further work is needed to quantify the effect this mismatch has on the tunability potential of the composite.

In closing, most importantly, since unit-cell-level differences can exist in the solid despite the same macroscopic shape, the study of designing phononic crystals of dielectric elastomers could unlock new ideas for tunability that cannot be achieved by other (e.g., mechanical) means.

7. References

1. Ainsworth, M., Wajid, Hafiz Abdul, “Optimally blended spectral-finite element scheme for wave propagation and nonstandard reduced integration” SIAM Journal on Numerical Analysis, Vol. 48, No. 1, 16.04.2010, p. 346-371.
2. Bertoldi, K.m Boyce, M., “Wave propagation and instabilities in monolithic and periodically structured elastomeric materials undergoing large deformations” Physical Review B 78, 2008.
3. Bustamante, R., Dorfmann, A., and Ogden, R.W. “Nonlinear electroelastostatics: a variational framework.” Zeitschrift für Angewandte Mathematik und Physik, 60(1), pp. 154-177. 2009.

4. Challa, S., “High-order accurate spectral elements for wave problems,” Advanced Computational Engineering and Mechanics Laboratory, Clemson University, Manuscript CMCU-98-03, August 1998. Master’s thesis by S. Challa, Clemson University, Dept. of Mechanical Engineering, August 1998.
5. Danielsson, M., Parks, D.M., Boyce, M.C., J. of the Mechanics and Physics of Solids, 50, 351-379, 2002.
6. Dorfmann, A., and Odgen, R.W., “Nonlinear electroelasticity,” Acta Mechanica 174, 167-183 (2005)
7. Dorfmann, A., and Ogden, R.W., “Nonlinear Theory of Electroelastic and Magnetoelastic Interactions,” Springer, New York, 2014. ISBN 978-1-4614-9595-6
8. Dorfmann, A., and Ogden, R.W., “Nonlinear electroelastostatics: Incremental equations and stability.” International Journal of Engineering Science, 48(1), pp. 1-14. 2010.
9. Guddati, M. and Yue, B., "Modified integration rules for reducing dispersion in finite element methods," Computer Methods in Applied Mechanics and Engineering, 193, pp. 275-287. 2004.
10. Henann, D., Chester, S., and Bertoldi, K., “Modeling of dielectric elastomers: Design of actuators and energy harvesting devices,” Journal of the Mechanics and Physics of Solids 61 (2013) 2047-2066.
11. Hughes, T.J.R., “The Finite Element Method: Linear Static and Dynamic Finite Element Analysis” Dover, Mineola, 2000.
12. Jandron, M., Henann, D., Cipolla, J., Ainsworth, M., “Optimally Blended Finite-Spectral Element Scheme for High Wavenumber Vibroacoustics,” 13th US National Congress on Computational Mechanics, San Diego, 2015.
13. Kushwaha, M., Halevi, P., Dobrzynski, L., Djafari-Rouhani, B., “Acoustic band structure of periodic elastic composites,” Phys. Rev. Lett. 71, 2002, 1993.
14. Kushwaha, M., Halevi, P., Martinez, G., “Theory of acoustic band structure of periodic elastic composites,” Phys. Rev. B. 49, 4, 1994.
15. Lai, Y., Zhang, X., Zhang, Z., “Engineering acoustic band gaps,” Applied Physics Letters, 79, 3223 (2001).
16. Matar, Robillard, Vasseur, Hladky-Hennion, Deymier, Pernod, Preobrazhensky, “Band gap tenability of magneto-elastic phononic crystal,” Appl. Phys. 111, 054901 (2012)
17. McMeeking, R.M., Landis, C.M., Jimenez, S., “A principle of virtual work for combined electrostatic and mechanical loading of materials,” International Journal of Non-Linear Mechanics, 42, 6, 831-838, 2007.
18. McMeeking, R.M., Landis, C.M, “Electrostatic forces and stored energy for deformable dielectric materials,” J Appl Mech 72:581-590.
19. Oh, Lee, Ma and Kim., “Active wave-guiding of piezoelectric phononic crystals,” Appl. Phys. Lett. 99, 083505 (2011)
20. Parsons, E., PhD thesis, MIT, 2006.
21. Pelrine, R., Kornbluh, R. and Joseph, J. “Electrostriction of polymer dielectrics with compliant electrodes as means of actuations,” Sens. Act. A Phys., 64, 77-85, 1998.

22. Pelrine, R., Kornbluh, R., Pei, Q., and Joseph J., "High-speed electrically actuated elastomers with strain greater than 100%," Science 287, 836-839, 2000.
23. Qian, Z., Jin, F., Li, F., Kishimoto, K., "Complete band gaps in two-dimensional piezoelectric phononic crystals with 1-3 connectivity family," International Journal of Solids and Structures, 45 (17), 4748-4755, 2008.
24. Shim J, Wang P, Bertoldi K. "Harnessing instability-induced pattern transformation to design tunable phononic crystals." International Journal of Solids and Structures. 58:52-61, 2015.
25. Shmuel, G., deBotton, G., "Band-gaps in electrostatically controlled dielectric laminates subjected to incremental shear strains," Journal of the Mechanics and Physics of Solids, 2012.
26. Shmuel, G., "Electrostatically tunable band gaps in finitely extensible dielectric elastomer fiber composites," Int. J. Solids Struct., 50:680-686, 2013.
27. Socrate, S., PhD thesis, MIT, 1995.
28. Srivastava, G.P., "The Physics of Phonons," CRC Press, ISBN 978-0852741535, 1990.
29. Suo, Z., Zhao, X., Greene, W.H. "A nonlinear field theory of deformable dielectrics," J Mech Phys Solids 56:467-486, 2008.
30. Tvergaard, V., "On localization in ductile materials containing spherical voids," Int. J. Fracture, 18 (3) 237-252, 1982.
31. Vasseur, Matar, Robillard, Hladky-Hennion, Deymier, "Band structures tenability of bulk 2D phononic crystals made of magneto-elastic materials," AIP Advances 1, 041904 (2011)
32. Vu, D., Steinmann,P., Possart, G., "Numerical modelling of non-linear electroelasticity," Int. J. Numer. Meth. Eng., 70 (2007), pp. 685–704.
33. Wang, Y., Li, F., Huang, W., Wang, Y., "Effects of inclusion shapes on the band gaps in two-dimensional piezoelectric phononic crystals," Journal of Physics Condensed Matter, 19, 2007.

8. Acknowledgements

This work is supported through the Naval Undersea Warfare Center In-house Laboratory Independent Research (ILIR) program managed by Mr. Neil Dubois. It is also being conducted as part of Ph.D. research at Brown University under the supervision of Prof. David Henann. Sponsor and mentor support is gratefully acknowledged.